

**Optical and Near Infrared Study of the Cepheus E outflow, a very
low excitation object.**

S. Ayala

Instituto de Astronomía, UNAM, Ap. 70-264, 04510 México, D. F., México

sayala@astrocu.unam.mx

A. Noriega-Crespo

SIRTF Science Center, IPAC, Caltech 100-22, Pasadena, CA 91125, USA

P. M. Garnavich

Harvard-Smithsonian Center for Astrophysics, 60 Garden St. (MS 42), Cambridge, MA 02138

S. Curiel and A.C. Raga

Instituto de Astronomía, UNAM, Ap. 70-264, 04510 México, D. F., México

K.-H. Böhm

Astronomy Department, University of Washington, Seattle, 98195

and

J. Raymond

Harvard-Smithsonian Center for Astrophysics, 60 Garden St. (MS 42), Cambridge, MA 02138

Received _____; accepted _____

ABSTRACT

We present images and spectra of the Cepheus E (Cep E) region at both optical and infrared wavelengths. Only the brightest region of the southern lobe of the Cep E outflow reveals optical emission, suggesting that the extinction close to the outflow source plays an important rôle in the observed difference between the optical and IR morphologies. Cep E is a unique object since it provides a link between the spectroscopic properties of the optical Herbig-Haro (HH) objects and those of deeply embedded outflows.

The observed H_2 infrared lines allow us to determine an excitation temperature of ~ 2300 K, an Ortho-to-Para ratio of ~ 3 , and an H_2 (1,0)/(2,1) S(1) line ratio of ~ 9 . These results are consistent with the values observed for HH objects with detected NIR emission lines, with shock excitation as the main mechanism for their formation, and also with the values observed for embedded, NIR flows.

The optical spectroscopic characteristics of Cep E (HH 377) appear to be similar to the ones of low excitation HH objects. However, the electron density determined from the $[\text{SII}]6731/6717$ line ratio for this object ($n_e = 4100 \text{ cm}^{-3}$), and the $[\text{OI}]6300/\text{H}\alpha$, $[\text{SII}](6717+6731)/\text{H}\alpha$ ratios are higher than the values of all of the previously studied low excitation HH objects. This result is likely to be the consequence of an anomalously high environmental density in the HH 377 outflow.

The ionization fraction obtained for HH 377 is $x_e \sim 1\%$. From this result, together with the observed $[\text{OI}]6300/\text{H}\alpha$ line ratio, we conclude that the observed $\text{H}\alpha$ line emission is collisionally excited. From a comparison with shock models, we also conclude that the extinction towards HH 377 is very low. Comparing the observed $\text{H}\beta$ and $\text{H}\alpha$ fluxes of HH 377 with model predictions, we determine a shock speed between 15 and 20 km s^{-1} , although somewhat higher velocities also produce spectra with line ratios that qualitatively agree with the observations of

HH 377.

Subject headings: jets and outflows – infrared, optical: interstellar: lines – ISM:
individual objects: Cepheus E, HH 377

1. Introduction

The Cepheus E (Cep E) outflow was first detected in the ^{12}CO J=1-0 transition in some of the early radio studies of star formation in molecular clouds . In his catalog of molecular outflows, Fukui (1989) first pointed out the presence of a bipolar, high velocity outflow in this region. The bipolar nature of Cep E became clear with the K' image of the molecular outflow obtained by Hodapp (1994), which included the stronger NIR H_2 lines, and revealed a relatively compact system (with a size of $\sim 1.5'$). Subsequent studies in the near/mid infrared have shown that the outflow is quite bright in the H_2 (1,0) S(1) 2.12 μm line, consistent with models of shock excited H_2 gas . Suttner et al. (1997) have used three-dimensional hydrodynamic simulations of highly collimated molecular outflows in order to model the morphology of Cep E. These simulations, however, required a very high density *in* the jet (10^5 cm^{-3}), which are not consistent with the hot and dense CO bullets recently found in the flow , with densities of $\sim 10^4 \text{ cm}^{-3}$.

The IRAS 23011+6126 source was originally identified as the main candidate for the outflow source. However, the presence of multiple outflows in near infrared and radio wavelengths indicates the existence of at least two sources, which have recently been confirmed by OVRO observations at 1.3 and 2.6mm . The sources are embedded and invisible at optical and near infrared wavelengths, and are likely to be Class I or Class 0 protostellar objects . In addition, Noriega-Crespo et al. (1998) detect one source at 6.9 μm using ISOCAM, which is well detected in all IRAS bands.

The present study has been motivated by the detection of emission at optical wavelengths in a small section of the southern lobe of the Cepheus E outflow by Noriega-Crespo (1997) and Devine et al. (1997). Noriega-Crespo (1997) mentions that $\text{H}\alpha$ and [SII] 6717/31 images reveal a compact knot which is the optical counterpart of the southern bowshock observed at 2 μm by Eislöffel et al. (1996). This optical knot has been named HH 377 .

In this study, we explore the link between the physical properties of the outflow as determined from optical imaging and spectroscopy, and compare these results with those obtained from observations in the near infrared. Our goal is to understand the development of very young stellar outflows (we notice that Cep E has a dynamical age of $\sim 3 \times 10^3$ years (Noriega-Crespo et al. 1998)) and the relationship between the mechanisms that produce the infrared and optical emission.

The paper is organized as follows. In Section 2 we describe the different observations obtained for this work, and comment on the reduction and calibration techniques. In Section 3, we present the results obtained from our infrared and optical observations. Finally, in Section 4 we compare the physical properties of Cepheus E deduced from the optical and the NIR observations with other Herbig Haro objects.

2. Observations

The optical and infrared observations were carried out at three different observatories. The log of the observations is presented in Table 1, and they are described in detail below.

2.1. Near Infrared Imaging and Spectroscopy

The NIR images of Cep E were obtained at two observatories. A set of images was obtained at the Apache Point Observatory 3.5m telescope (APO 3.5m) with a 256×256 array at f/5 and a $0.482''$ per pixel scale. The central wavelengths (and bandpass) of these images were at $2.12\mu\text{m}$ (1%), for the H_2 (1,0) S(1) line, and $2.22\mu\text{m}$ (4%) for the nearby continuum.

Another set of images was obtained at the Observatorio Astronómico Nacional at San Pedro Mártir 2.1m telescope (OAN SPM 2.1m) with the IR camera/spectrometer CAMILA, which has a 256×256 array providing a $0.85''$ /pixel scale at f/4.5. The central wavelengths

(and bandpass) of the filters used to obtain these images were $2.12\mu\text{m}$ (1%), $2.25\mu\text{m}$ (1%) for the H_2 (2,1) line, cK (2%) and $\text{Br}\gamma$ $2.16\mu\text{m}$.

The frames were flattened with a combination of low and high illumination sky flats obtained at sunset. The data were processed by subtracting a median-filtered image of nearby sky frames taken with the same integration time and with offsets between 30 and $100''$. Bad pixels were removed with standard techniques.

The processing of our frames was done with Image Reduction and Analysis Facility (IRAF)¹ based programs. For each filter, 10 (APO data) and 9 (OAN SPM data) overlapping frames were taken (see Table 1 for the integration times). The frames were aligned using several field stars, and median combined into the final images. The image scale and orientation were calculated using 7 common stars between the IR frames and an optical image from the Digitized Sky Survey, with a resultant mean uncertainty of less than one arcsecond in the positions.

The NIR spectra were obtained with the Multiple Mirror Telescope Observatory (MMTO). The set of H and K band spectra of the North and South lobes of Cep E were taken with the Rieke FSPEC IR spectrometer. The slit was aligned in the E-W direction in both lobes (see Figure 1) and alternate exposures were chopped between the source and the local sky. The atmospheric absorption and sensitivity variation along the dispersion were corrected by observing a bright late-F type star at nearly the same airmass as the target data. The spectra were obtained with a $1.0''$ wide slit, and the extraction was done over an area of $4.0 (')^2$ for each outflow lobe.

¹IRAF is distributed by the National Optical Astronomy Observatory (NOAO), which is operated by the Association of Universities for Research in Astronomy (AURA), Inc. under cooperative agreement with the National Science Foundation

2.2. Optical Imaging and Spectroscopy

As mentioned above, the south lobe of Cep E is detected at optical wavelengths, in the $H\alpha$ and [S II] 6717/31 lines. Our narrow band images in $H\alpha$ and [S II] were obtained with the 1.2m telescope at Fred Lawrence Whipple Observatory (FLWO 1.2m). A thinned, back-side illuminated, AR coated Loral 2048 \times 2048 CCD was used with a plate scale of 0.315 "/pix. The central wavelength and FWHM of the narrow band $H\alpha$, [S II] and continuum filters are, respectively, $\lambda 6563$, 25 Å, $\lambda 6724$, 50 Å, and $\lambda 6950$, 400 Å. The CCD images were binned two by two giving a 0.63 "/pix scale, and were processed using IRAF, in the standard way. For each filter, the final image corresponds to the median-filter of three 600 seconds frames.

A low resolution, long-slit spectrum over a $\sim 4500 - 7000$ Å wavelength range with $\simeq 2$ Å/pix was obtained at the MMT telescope. The spectrum was reduced using IRAF and flux calibrated using the standard star HR8687.

Two long-slit spectra were also obtained at the FLWO 1.5m telescope with the FAST spectrometer, using a Loral 512 \times 2688 coated CCD with 15 μ m pixels. Two different spectral resolutions (1.49 Å/pix and 0.75 Å/pix) were used to cover the wavelength ranges of 5500-7000 Å and 6200-6800 Å. The slit width was 1.1" and the slit was oriented N-S. The spectra were flux calibrated with the standard stars BD284211 and G191B2B.

3. Results

3.1. Infrared excitation

The complex structure shown by Cepheus E in vibrationally excited molecular hydrogen lines has been described in previous papers. Figure 1 shows a section of our H_2 (1,0) S(1) continuum subtracted image, in which we plot the slit positions used to obtain the infrared spectra.

Using the H_2 $\lambda 2.121\mu\text{m}$ and $\lambda 2.248\mu\text{m}$ images we construct a (1,0)/(2,1) S(1) line ratio image. The line ratio is nearly constant throughout the outflow with a mean value of 10 ± 5 . This result is completely consistent with previous results on this object.

In our Bracket γ + continuum image we have detected emission extending over both lobes. The distribution of this emission is very similar to the one of the continuum cK frame. Because of this similarity we suspect that the flux detected in our $\text{Br}\gamma$ frame is on the whole continuum emission. This interpretation is consistent with the absence of $\text{Br}\gamma$ line in the spectra obtained for the brightest knots of both lobes (see Figure 2).

The spatially integrated spectra in the H and K bands of the northern and southern lobes of Cepheus E are shown in Figure 2. These spectra were constructed by integrating along the slit over the width of the lobes ($\sim 4''$) for the slit positions indicated in Figure 1. The identified and measured H_2 lines in these bands are indicated on the plots at the expected wavelengths. Note that no $\text{Br}\gamma$ ($\lambda 2.166\mu\text{m}$) line emission is detected in these slit positions, which correspond to the brightest knots of each lobe. Table 2 lists the H_2 transitions (column 1), their wavelengths (column 2; see Black & van Dishoeck, 1987); the energy $E(v, J)$ of the upper level (column 3, Dabrowski 1984), and the measured fluxes of the identified H_2 lines (columns 4 and 5 for the N and S lobes, respectively). From these spectra we determine a $\Delta V_r \sim 90 \pm 30 \text{ km s}^{-1}$ between the northern and southern lobes, and the south lobe shows a blueshift. Comparing the fluxes for (1,0) S(1) and (2,1) S(1) lines from our spectra with previous values obtained from surface photometry for these transitions, we find that our (1,0) S(1) flux values are lower with respect of the Eisloffel et al. values, by a factor ~ 2 . Whereas in the case of (2,1) S(1) fluxes the present and previous measurements are completely consistent.

We have estimated the column densities $N(v, J)$ assuming that the lines are optically thin, in order to determine the excitation temperature, T_{exc} , of the warm molecular gas in each lobe. Under conditions of local thermodynamic equilibrium (LTE), the relationship between column density and energy of the upper level $E(v, J)$, is $\ln[N(v, J)/g_J] = E(v, J)/kT_{exc} + C$;

where g_J is the degeneracy of the corresponding level, k is the Boltzmann constant, and C is a constant.

Figure 3 shows the excitation diagrams for Cep E, South and North lobes. We plot $N(v, J)/g_J$ versus energy $E(v, J)$ of the level for each lobe using the fluxes listed in Table 2². In each panel, the transitions between the (1,0) vibrational levels are plotted with solid squares, the ones between the (2,1) levels with triangles and the (3,2) levels with solid circles. The excitation temperatures, T_{exc} (calculated from linear fits), are 2340 ± 100 for the South lobe and 2260 ± 110 for the North lobe.

In the case of a purely thermal population caused by a shock, it is expected that a single smooth curve should fit all of the transitions in the excitation diagrams, meaning that a single temperature describes the excitation. On the other hand, in the case of fluorescent H_2 emission, the points within vibrational levels are expected to be aligned on separate curves, resulting in different temperatures for different vibrational levels. Intermediate cases in which there is a combination of both excitation mechanisms are also possible (Fernandes & Brand 1995; Fernandes, Brand & Burton 1995).

The derived excitation temperatures, T_{exc} , for both lobes of Cepheus E are consistent with the T_{exc} measured in HH objects ($T_{exc} \sim 2000$ K, Gredel 1994), whereas the excitation temperatures observed in collisionally plus fluorescent excited objects have $T_{exc} \sim 3000$ values (Fernandes, Brand & Burton 1997). However, in Figure 3 there are real dispersions around the dashed lines drawn in each panel. If we fit the points from different vibrational levels separately, there are slight differences between these fits and the fit obtained considering all of the vibrational levels together.

²The excitation diagrams do not include the very weak H_2 (3,2) S(5) line presented in Table 2. This transition shows a bigger column density than expected, which causes great dispersion in the estimation of the excitation temperature, so we have excluded it from our analysis.

We have computed the rotational excitation temperatures using the transitions within different vibrational levels. The resulting temperatures are listed in Table 3. In order to explore the excitation mechanisms occurring in the Cep E outflow, we have computed some interesting line ratios (with the fluxes presented in Table 2), which are also listed in Table 3. This table gives the vibrational levels (column 1), the rotational levels of the transitions used for the ratios (column 2), the rotational temperature T_{rot} derived from these transitions (column 3), the empirical Ortho/Para ratio derived for each vibrational level (column 4), and the (1,0)/(2,1) S(1) ratio derived for each spectrum (column 5).

As we can see, for both lobes of Cepheus E the rotational excitation temperatures (Table 3) are lower than the calculated vibrational temperature T_{exc} (see Figure 3). Though different from T_{exc} , the rotational temperatures are still consistent with the temperatures observed in collisionally excited objects. We should note that the vibrational level (2,1) shows the lowest rotational temperature.

We find that the values obtained for the Ortho/Para ratio are similar for the two lobes of Cepheus E. For the Northern lobe there is a higher dispersion for this ratio between the different vibrational levels. This is a result of the dispersion in the points corresponding to the (2,1) and (3,2) levels (see top panel of Figure 3). This dispersion is probably a result of the fact that the spectrum of the Northern lobe is fainter. We conclude that the Ortho/Para ratios estimated for Cep E are completely consistent with the LTE value of 3, as expected for collisional excitation.

We analyzed the behavior of the (1,0)/(2,1) S(1) line ratio. Column (5) of Table 3 gives the 8.50 ± 1.10 and 9.40 ± 1.30 values obtained for the Northern and Southern lobes, respectively. These values are consistent with the result obtained from the (1,0)/(2,1) S(1) ratio image (see above), and slightly lower than the ones measured from (1,0)/(2,1) S(1) frames by Eislöffel et al. 1996. Also, the obtained (1,0)/(2,1) S(1) line ratio is completely consistent with the value of 10 expected for collisional excited H_2 lines, and does not approach

the ~ 1.7 value expected for fluorescent excitation .

A detailed analysis on the K-band spectra of Cep E has already been performed by Ladd & Hoddap (1997). They found that a C-type shock with 35 km/s can explain the K-band H_2 fluxes and ratios. This is consistent with the ISO Long Wavelength Spectrometer observations, which show several emission lines from H_2O transitions , as it is expected from molecular C-type shocks .

In Cep E we find a similar situation as in other Herbig-Haro objects (e.g. HH 1-2; Davis et al. 1994; Noriega-Crespo & Garnavich 1994) where J-type (inferred from the optical spectra) and C-type (inferred from the IR spectral) seem to coexist spatially. The case of Cep E is particularly interesting since it appears to be a very young outflow, based on its compact size and the age of its exciting source. If so, a better interpretation of its spectral properties may require molecular time dependent shock models, which are currently under development .

3.2. The optical morphology

In contrast with the complex structure of the H_2 outflow, the optical emission consists of only one compact knot (HH 377), which approximately coincides with the brighter H_2 knot of the southern lobe . In Figure 4 we present an H_2 1-0 S(1) contour map of Cepheus E, overlaid on grey-scale and contour representations of our optical images. Panel *a*) shows grey-scale representations of the $H\alpha$ image and panel *b*) of the [S II]6717,6731 image. Panels *c*) and *d*) show the $H\alpha$ and [S II]6717,6731 images (respectively) as contour maps, over a smaller angular area. These maps clearly show the coincidence between the optical knot and the brightest region of the southern lobe of the IR flow.

In Figure 4, we see that a star still remains in the $H\alpha$ continuum subtracted image (panel *a*), to the west of HH 377. This stellar emission could indicate either that the star has intrinsic $H\alpha$ emission, or that the stellar continuum has a substantially different slope than the continua

of the stars used to obtain the relative scaling between the $H\alpha$ and the continuum frames.

The $H\alpha$ and [S II] morphologies of HH 377 are different, the knot is resolved in both images, but it is clearly brighter and more compact in the [S II] image. In our [S II] image, HH 377 has an angular size of $5''$, resulting in a diameter of 0.02 pc (at a distance of 0.75 kpc, Hodapp 1994) for the knot. We can also see that the morphology of the southern lobe of Cep E is qualitatively consistent with a bow-shock model, in which the wings have a stronger contribution of H_2 emission, while the head is dominated by the atomic/ionic emission.

Finally, in Figure 4 (panel *b*), we show the two slit positions used to obtain the spectra described in the following section.

3.3. Optical spectroscopic characteristics

We have obtained two spectra (intermediate and low resolution) with the N-S slit (see Figure 4), and a single (low resolution) spectrum with the E-W slit (see the discussion in section 2.2). Our spectrophotometric data gives us the optical excitation conditions of HH 377. Figure 5 shows the flux-calibrated spectrum, extracted from a $4''^2$ in the E-W oriented slit (see panel *b* of Figure 4). The results obtained for the relative fluxes with and without reddening correction (for our three spectra) are listed in Table 4. Column 1 gives the identification of the detected lines, column 2 lists the observed (F) and reddening-corrected (F_0) relative fluxes for the E-W slit, column 3 and 4 list the fluxes from the N-S slit at low and intermediate resolutions, respectively. The determination of the value of $E(B - V)$ that we have used is discussed in the following section. In addition, the radial velocity estimate from these spectra is $V_r = -70 \pm 10 \text{ km s}^{-1}$.

From the spectrum with larger wavelength coverage (see Table 4 and Figure 4), we can see that [NI]5200 is greater than $H\beta$ and that the [SII]6717/31 and [OI]6300/64 fluxes are stronger than $H\alpha$. No [OIII]5007 nor [NII]6548,83 emission is detected. These observed characteristics

are typical of low excitation Herbig-Haro objects.

Finally, we use the [SII] 6731/6717 line ratio to compute an electron density $n_e = 4100 \text{ cm}^{-3}$ (assuming an electron temperature $T_e = 10^4 \text{ K}$). As discussed in the following section, this result is particularly interesting.

4. Discussion: Cep E as a low excitation Herbig-Haro object

As the limited wavelength coverage of our spectra does not allow us to use Miller’s (1968) method, we have determined the reddening by assuming that the intrinsic (dereddened) Balmer decrement has a $H\alpha/H\beta=3$, (i.e., a recombination cascade value). Using the measured $H\alpha/H\beta=7.75$ ratio and the standard, $R_V = 3.1$ ISM reddening curve of Mathis (1990), we obtain $E(B - V) = 0.88 \pm 0.12$ (corresponding to an $A_V = 2.72 \pm 0.38$ optical extinction). This method is of course uncertain for the case of Cepheus E (and other HH objects) since it is expected that in the case of low velocity shocks the Balmer decrement could differ substantially from the recombination value. We have used the optical total-to-selective ratio $R_V = A(V)/E(B - V) = 3.1$ which is frequently used in these cases and appears to be the most appropriate for HH objects .

In Table 5 we present line ratios observed for Cep E from the fluxes given in column 2 of Table 4. The optical spectroscopic characteristics of HH 377 (Cep E) identify it as a low excitation object. Indeed, we find that the excitation of this object appears to be anomalously low, compared to other low excitation HH objects. For example, most of the observed line ratios obtained for HH 377 are consistent with the ones observed in other low excitation objects, except for the [SII](6717+6731)/ $H\alpha$ ratio. For HH 377, this ratio is a factor of ~ 3 higher than the corresponding values for the low excitation HH objects (HH 7, HH 11, HH34(jet), HH 47A, HH 111 D-J, HH 125 I and HH 128), this fact is clear in second panel top to bottom, Figure 6. The [SII] 6731/6717 ratio is also the highest one observed (with a value

of 0.59 ± 0.09). This line ratio implies an electron density $n_e \approx 4100 \text{ cm}^{-3}$, which is the largest n_e measured for any previously detected, low excitation HH object (see Figure 6, bottom panel). The electron density is relatively high and comparable to the densities measured in high excitation HH objects. The low excitation in Cep E suggests, however, a low ionization fraction and therefore a higher gas density than usual.

Following Raga et al. (1996), we compare the line ratios of Cep E (HH 377) with those obtained for other HH objects. We refer the line ratios to the [OI]6300/H α ratio, which is different from Raga et al.(1996), who plot all of the line ratios versus the [N I](5198+5200)/H β line ratio. We have done this because the [N I] lines have a very low critical density ($\sim 2900 \text{ cm}^{-3}$), so that collisional quenching will occur in Cep E (while not in the other low excitation HH objects).

In Figure 6 we plot the [NI](5198+5200)/H β , [SII](6717+6731)/H α , and [SII]6731/6717 line ratios (and also, the electron density n_e) as a function of the [OI]6300/H α ratio, indicating the values that correspond to high, intermediate and low excitation HH objects. The line ratios for Cep E are indicated with an asterisk. In this Figure we can see the anomalous line ratios, specially the [SII](6717+6731)/H α ratio and electron density (n_e) obtained for Cep E, in contrast to other low excitation HH objects.

Let us now compare the line ratios of HH 377 (Cep E) with shock model predictions. The plane shock models of Hartigan et al. (1994) do show high [SII](6717+6731)/H α ratios, in better agreement with the observations of HH 377. From this work, we list the range of line ratios obtained for models of shock velocities in the $v_s = 20\text{-}30 \text{ km s}^{-1}$ range (labeled J4.20-30 in Table 5), and models with $v_s = 30\text{-}40 \text{ km s}^{-1}$ (labeled J4.30-40), in both cases with a high pre-shock density $n_0 = 10^4 \text{ cm}^{-3}$ and magnetic fields between 30 and 300 μG . We have also listed the line ratios for models with $v_s = 30 - 40 \text{ km s}^{-1}$ and lower pre-shock density ($n_0 = 10^2 \text{ cm}^{-3}$) and the same magnetic field range than the models described above.

We can see that the J4.20-30 models are the most successful at reproducing the line ratios observed in Cep E. In particular, these shock models do reproduce the observed $[\text{SII}](6717+6731)/\text{H}\alpha$ and $[\text{S II}]6731/6717$ ratios. Interestingly, these models also predict an $\text{H}\alpha/\text{H}\beta \sim 6$ Balmer decrement.

This result seems to favor shock models with a very low shock velocity and high pre-shock density in order to reproduce the observed optical line ratios. One has to keep in mind that J-type shocks in molecular gas are restricted to velocities $\sim 30 - 50 \text{ km s}^{-1}$ (Hollenbach & McKee 1989) in order to not dissociate H_2 , and so at first order the simple J-type atomic/ionic plane parallel shock models are consistent with the rich H_2 spectra observed in Cep E.

We have estimated a new value for the extinction to Cep E using the $\text{H}\alpha/\text{H}\beta \sim 6$ predicted by these models, obtaining $E(B - V) \sim 0.24$ (corresponding to an $A_V \sim 0.77$ optical extinction). However, it is important to note that for Cep E, only the brightest region of the southern lobe of the H_2 outflow reveals optical emission. This fact suggests that a high extinction close the outflow region could explain the observed differences between the optical and IR morphologies.

Lefloch et al. (1996) determined values for the optical extinction using observations of the continuum emission of Cepheus E outflow at 1.25 mm. They reported $A_V = 3.2, 3.4$ for the northern and southern H_2 lobes, respectively (on the same bright infrared knots which we analyze in this paper). These values are similar to our first A_V estimation from the recombination cascade Balmer decrement for HH377, in the beginning of this section. The result implies a similar extinction for both infrared lobes. On the other hand, Noriega-Crespo et al. 1998 find a constant $v = 00 \text{ S}(3)/0-0 \text{ S}(5)$ ratio that also indicates the lack of a steep extinction gradient between the north and south lobes and that the extinction is mostly important around IRAS 23011+6126. This is interesting because we know that the south lobe is visible at optical wavelengths (Noriega-Crespo 1997), while the north lobe is not. It would be interesting to obtain extinction values for HH 377 through Miller’s method. This would

give a realistic value for the fraction of the extinction which arises in the vicinity of the object, and would help to discriminate between and/or to constrain the different shock models.

4.1. The ionization fraction in HH 377

In order to estimate the ionization fraction in the southern lobe of Cep E (HH 377) we use the [OI]6300/H α ratio, which for recombination H α is given by

$$\frac{I([O\ I] 6300)}{I(H\alpha)} = X(O) \frac{n(O\ I)/n(O)}{n(H^+)/n(H)} \frac{q_{ex}(6300)}{\alpha(H\alpha)}, \quad (1)$$

where $X(O)$ is the oxygen abundance, $q_{ex}(6300)$ is the excitation rate coefficient for [O I] 6300, and $\alpha(H\alpha)$ is the effective recombination rate coefficient for H α .

For low excitation HH objects we expect electron temperatures lower than 10^4 K (Bacciotti & Eisloffel, 1999). If we assume that $T_e \sim 5000$ K, we obtain $q_{ex}(6300) \sim 4 \times 10^{-10}$ cm³ s⁻¹, and $\alpha(H\alpha) \sim 2 \times 10^{-13}$ cm³ s⁻¹. For an oxygen abundance of $X(O) = 8 \times 10^{-4}$, and the $I([O\ I] 6300)/I(H\alpha) = 2.5$ ratio observed in HH 377, from eq. (1) we obtain $[n(O\ I)/n(O)] / [n(H^+)/n(H)] = 1.6$; which implies that the gas is roughly 50% ionized.

On the other hand, we can also estimate the ionization fraction, x_e , from the nitrogen lines using the ratio

$$\frac{I([N\ I] 5200)}{I([N\ II] 6584)} \sim 0.13 \frac{n(N\ I)}{n(N\ II)}. \quad (2)$$

Using the $I([N\ I] 5200)/I([N\ II] 6584) > 10$ limit deduced from the spectrum of HH 377 (shown in Figure 5), we then obtain $n(N\ I)/n(N\ II) < 0.01$, which implies that the ionization fraction is less than 1%. A similar value is obtained for the [SII]-weighted ionization fraction using the different line ratios in the diagrams shown in Hartigan et al. (1994, Figures 3 to 5), for the models J4.20-30 (see above).

From the discrepancy between this low ionization fraction and the much higher one deduced from eq. (1), we conclude that the H α line has to be collisionally excited. We

therefore conclude that the low reddening for HH 377 obtained through the shock models (in which the Balmer decrement is about 6), is probably correct. If we consider the compression produced by the shock (which is approximately equal to the square of the Mach number) and the ionization fraction deduced above we can estimate the pre-shock density. The shock velocity estimated for HH 377 (see section 4.0) implicates a Mach number of $M^2 \sim 10$. Using an ionization fraction $x_e \sim 1\%$ and considering that $N_e \sim 10^4 \text{ cm}^{-3}$, we then obtain a pre-shock density $\sim 10^5 \text{ cm}^{-3}$. Note that this total particle density results very high at the distance from the outflow source, and it is very unusual for HH objects with any excitation level.

4.2. The absolute fluxes in HH 377.

From the Hartigan et al. (1994) shock models with $v = 20 \text{ km s}^{-1}$ and pre-shock density of 10^4 cm^{-3} , one obtains an $\text{H}\alpha/\text{H}\beta \sim 9$ and fluxes of $\text{H}\beta = 1.0 \times 10^{-5}$ and $\text{H}\alpha = 9.0 \times 10^{-5} \text{ ergs cm}^{-2} \text{ s}^{-1}$, out of the front of the shock. For a pre-shock density of 10^5 cm^{-3} one would have fluxes larger by about an order of magnitude. This gives $\text{H}\beta = 1.6 \times 10^{-5}$ and $\text{H}\alpha = 1.5 \times 10^{-4} \text{ ergs cm}^{-2} \text{ s}^{-1} \text{ steradian}^{-1}$, when applying the solid angle. Using an area of $1.5'' \times 4''$ (see column 2 of Table 4), we obtain that the predicted fluxes for $\text{H}\beta$ and $\text{H}\alpha$ are 2.3×10^{-15} and $2.1 \times 10^{-14} \text{ ergs cm}^{-2} \text{ s}^{-1}$, respectively. These fluxes are about 6 times larger than the observed fluxes (see Table 4). However, the Balmer line fluxes of the Hartigan et al. (1994) models are extremely steep functions of shock speed, so a shock speed between 15 and 20 km s^{-1} would give the correct total fluxes.

Finally, we must ask how the optical emission and the molecular hydrogen emission are related in this dense, low excitation HH object. Hartigan et al. (1996) discuss the possible morphologies. One option is a bow shock which has a J-shock nature at its tip (producing

optical emission) with C-shocks or turbulent entrainment producing the H_2 emission from the bow shock wings. Another is a C-shock in the ambient cloud accompanied by a J-shock at the Mach disk in the jet material. A third possibility is a J-shock with an MHD precursor which produces both optical and IR emission at the bow shock tip. Unfortunately, the high density of Cep E, the emitting regions extremely thin, so that it is difficult to use morphology to distinguish among the possibilities.

The various combinations of C- and J-shock models have many free parameters, so that it is also difficult to use spectra to distinguish among them. One interesting comparison, however, is the ratio between IR and optical luminosities. If the optical emission arises from the Mach disk and the H_2 emission from the bow shock, and if the jet and ambient densities are not too drastically different, the luminosities should be comparable (e.g Hartigan 1989). The C-shock luminosity emerges mostly in the near IR lines we observe, while according to the slow J-shock models, the luminosity is around 1000 times the $\text{H}\beta$ luminosity, with most of the energy emerging in $\text{Ly}\alpha$ (cf. the 15 and 20 km s^{-1} models of Hartigan et al. 1994). Thus

$$F_{\text{IR}} \sim 7 \times 10^{-12} \text{ ergs cm}^{-2} \text{ s}^{-1}, \quad (3)$$

calculated from data in Table 2. And $F(\text{H}\alpha) \sim 3 \times 10^{-14} \text{ ergs cm}^{-2} \text{ s}^{-1}$ for a smaller reddening than the 0.88 (Table 3), then we can estimated

$$F(\text{Ly}\alpha) \sim 1000 F(\text{H}\beta) \sim 150 F(\text{H}\alpha) \sim 4.5 \times 10^{-12} \text{ ergs cm}^{-2} \text{ s}^{-1}. \quad (4)$$

Thus it seems as though the J-shock is within an order of magnitude of the C-shock luminosity, so the possibility that the Mach disk makes the optical emission and the bow shock makes the IR emission is reasonable.

5. Conclusions

We have carried out a spectroscopic and imaging study of the molecular hydrogen and optical atomic/ionized emission in the Cepheus E outflow. Our main results are:

- For deriving the excitation state of molecular gas in Cep E we use line ratios from our H-band and K-band spectra. We find that $T_{exc} = 2260 \pm 110$ and 2340 ± 100 K for the northern and southern lobes, respectively, which are consistent with the T_{exc} measured in other HH objects. The (1,0)/(2,1) S(1) ratios (8.50 and 9.40), and the Ortho/Para ratios (values ~ 3) in both lobes are also consistent with the values observed in collisionally excited objects.
- Contrasting with the complex structure of the H_2 outflow, the optical emission is a compact, well resolved knot (HH 377), that nearly coincides with the southern NIR lobe. The [S II] emission of HH 377 is clearly brighter and more compact than the $H\alpha$ emission and its angular size is about 0.02 pc (at a distance of 0.75 kpc). The [S II] and $H\alpha$ peak emission spatially coincide and appear offset a few arcseconds upstream from the H_2 peak emission.
- Our spectroscopic optical analysis reveals that HH 377 has characteristics typical of low excitation Herbig-Haro objects. This is confirmed when comparing the relative fluxes of HH 377 with those of other HH objects using line ratio diagrams. However, HH 377 presents anomalous [SII](6717+6731)/ $H\alpha$ line ratio, larger than those obtained for objects classified as low excitation HH objects. The electron density, $n_e = 4100 \text{ cm}^{-3}$, determined for this object from [SII] lines would be the highest density measured in low excitation HH objects. This value is similar to the electronic densities measured in high excitation HH objects.
- We estimate an ionization fraction $x_e \sim 1\%$ for HH 377. Together with the observed [OI]6300/ $H\alpha$ ratio, this result implies that the observed $H\alpha$ line has to be collisionally excited. This result supports the low reddening obtained for HH 377 obtained through the shock models. Using this ionization fraction, a post-shock electron density $N_e \sim 10^4 \text{ cm}^{-3}$ and a compression of ~ 10 , we obtain a pre-shock density $\sim 10^5 \text{ cm}^{-3}$ for HH 377. This exceptionally

high pre-shock density is very unusual for HH objects.

- From the shock model predictions and the $H\beta$ and $H\alpha$ observed fluxes, we find that a shock speed between 15 and 20 km s⁻¹ gives the correct total fluxes for HH 377. This velocity appears to be somewhat lower than the one deduced from the observed line ratios.

- From a comparison between optical and infrared luminosities in HH 377 we find the possibility that the Mach disk produces the optical emission and the bow shock produces the IR emission.

- We have determined a visual extinction $A_V = 2.72$ ($E(B - V)=0.88$) assuming a recombination cascade $H\alpha/H\beta=3$ Balmer decrement. If we use the $H\alpha/H\beta \sim 6$ decrement predicted by the preferred shock wave models we obtain an $A_V \sim 0.77$ ($E(B - V) \sim 0.24$) extinction. Interestingly, Lefloch et al. (1996) have obtained an $A_V = 3.4$ from the mm continuum of the southern lobe of the Cep E outflow, in qualitatively good agreement with the extinction obtained assuming $H\alpha/H\beta=3$ (see above). This confusing situation involving the optical extinction towards HH 377 and the Balmer decrement predicted from low velocity shock models could be clarified with future observations of the blue and IR [SII] lines (or, alternatively, the IR [Fe II] lines) of this object, in order to have a model-independent determination of the extinction. The overall extinction along the Cep E flow varies drastically. One could speculate different reasons (e.g. a large inclination with respect to the plane of the sky, a dense molecular gas core surrounding the source with a rapidly decreasing density profile and/or a non-homogeneous ISM). We can not answer this question with our present data.

- Comparing the *optical* line ratios observed in south lobe of Cep E to atomic/ionic plane-parallel shock models (J-type) presented in the literature (Hartigan et al. 1994), we find that low velocity ($v_s = 20$ -30) shocks are the closest to reproduce the observations. These models have a high pre-shock density ($n_0 = 10^4$ cm⁻³), and magnetic fields between

30 and 300 μG . These conditions (high density, low ionization fraction and strong magnetic field) are quite appropriate for the development of molecular C-type shock as well. Previous comparisons of the H_2 near-ir spectra with molecular shocks (Ladd & Hodapp, 1997), indeed indicated a preference for C-type shocks with $\sim 35 \text{ km s}^{-1}$. Preliminary results from ISO Long Wavelength Spectrometer (50 - 200 μm) support also this view, given Cep E rich H_2O spectra (Noriega-Crespo 2000), a characteristic signature for C-type shocks (Kaufman & Neufeld 1996ab; Noriega-Crespo et al. 2000)

- Finally, our analysis seems to confirm that Cep E corresponds to an outflow in its earliest developing phases. Its short dynamical age of few 10^3 yrs, the high gas density estimated (at least 10^5 cm^{-3}) and the inhomogeneous nature of its extinction, suggest that the outflow is breaking through its placental molecular core.

This work was supported by DGAPA grant IN109297 and CONACYT grant 26833-E and 27546-E. S.A. & S.C. would like to thank César Briseño for obtaining some of the optical images. A.N.-C. & P.M.G thank Nichole King for her help on the observations. The FSPEC IR spectra were obtained with the help of Marcia Rieke & George Rieke at the MMT0, A.N.-C. & P.M.G are grateful to both. K.H.B. has been supported by NSF grant AST 9729096. Last but not least, we thank the referee David Devine for his comments and careful reading of our manuscript.

REFERENCES

- André, P., Ward-Thompson, D., & Barsony, M. 1993, *ApJ*, 406, 122
- Bacciotti, F. and Eisloffel, J. 1999, *A&A*, 342, 717.
- Black, J.H., and van Dishoeck, E.F. 1987, *ApJ*, 322, 412
- Böhm, K.-H., Raga, A.C., & Binette, L. 1991, *PASP*, 103, 85.
- Burton, M.G., Hollenbach, D.J. and Tielens A.G.G.M., 1990, *ApJ*, 365, 620
- Cruz-Gonzales, I.; Carrasco, L.; Ruiz, E.; Leija-Salas, L.; Skrutskie, M.; Meyer, M. R.; Sotelo, P.; Barbosa, P.; Gutierrez, L.; Iriarte, A.; Cobos, F. J.; Bernal, A.; Sanchez, B.; Valdez, J.; Arguelles, S.; Conconi, P. 1994, *Proc SPIE*, 2198, 774
- Dabrowski, I. 1984, *Canadian J. Phys.*, 62, 1639
- Davis, C.J., Eisloffel, J., & Ray, T.P. 1994, *ApJL*, 426, 93
- Devine, D., Reipurth B., & Bally J. 1997 in “Low Mass Star Formation from Infall to Outflow”
Ed. F. Malbet & A. Castets, p91
- Eisloffel, J., Smith, M.D., Davis, C.J., & Ray, T.P. 1996, *AJ*, 112, 2086
- Fernandes, A. and Brand, P. 1995, *MNRAS*, 274, 639
- Fernandes, A., Brand, P. and Burton, M., 1995, *Ap&SS*, 233. 45
- Fernandes, A., Brand, P. and Burton, M., 1997, *MNRAS*, 290, 216
- Flower, R.D., & Pineau des Forets, G. 1999, *MNRAS*, 308, 271
- Fukui, Y. 1989, in “Low Mass Star Formation and Pre-Main Sequence Objects”, ESO 1989,
ed. B. Reipurth, p95

- Gredel, R. 1994 A&A, 292,580
- Hartigan, P. 1989 ApJ, 339, 987.
- Hartigan, P., Morse, J.A. and Raymond, J. 1994, Ap J, 436, 125
- Hartigan, P., Carpenter, J.M., Dougados, C., and Skrutskie, M.F. 1996, AJ, 111, 1278
- Hatchell, J. Fuller, G.A. & Ladd, E.F. 1999, A&A, 346, 278.
- Hodapp, K.-W. 1994, ApJSS, 94, 615
- Hollenbach, D., McKee, C.F. 1989, ApJ, 342, 306
- Kaufman, M.J., & Neufeld, D.A. 1996a, ApJ, 456, 611
- Kaufman, M.J., & Neufeld, D.A. 1996b, ApJ, 456, 250
- Ladd, F.E., & Hodapp, K.-W. 1997, ApJ, 474, 749
- Leffloch, B., Eisloffel, J., & Lazareff, B. 1996, A&A, 313, L17
- Mathis, J.S. 1990, ARAA, 28, 48
- Miller, J.S. 1968, ApJ, 154, L57
- Noriega-Crespo, A. 1997, in “Herbig-Haro Flows and the Birth of low Mass Stars”, eds. B. Reipurth & C. Bertout, p103
- Noriega-Crespo, A. & Garnavich, P.M. 1994 AJ, 108, 1432
- Noriega-Crespo, A., Garnavich, P. M. & Molinari, S. 1998, AJ, 116, 1388
- Noriega-Crespo A. 2000 in ”ISO Beyond the Peaks. The 2nd ISO workshop on analytical spectroscopy”, A. Salama & M. Kessler, eds. ESA (in press)
- Noriega-Crespo, A., Moro-Martin, A., Cernicharo, P. & Molinari, S. 2000, in preparation.

- Raga, A.C., Böhm, K.-H. and Cantó, J. 1996, *Rev Mex Astron Astrof*, 32, 161
- Sargent, A. I. 1977, *ApJ*, 218, 736
- Schwartz, R.D., Schultz, A.S.B., Cohen, M., Williams, P.D. 1995, *ApJ*, 446, 318.
- Smith M.D. 1009, *A&A*, 296, 789.
- Suttner, G., Smith, M.D., Yorke, H.W., & Zinnecker, H. 1997, *A&A*, 318, 595
- Testi, L., Private Communication

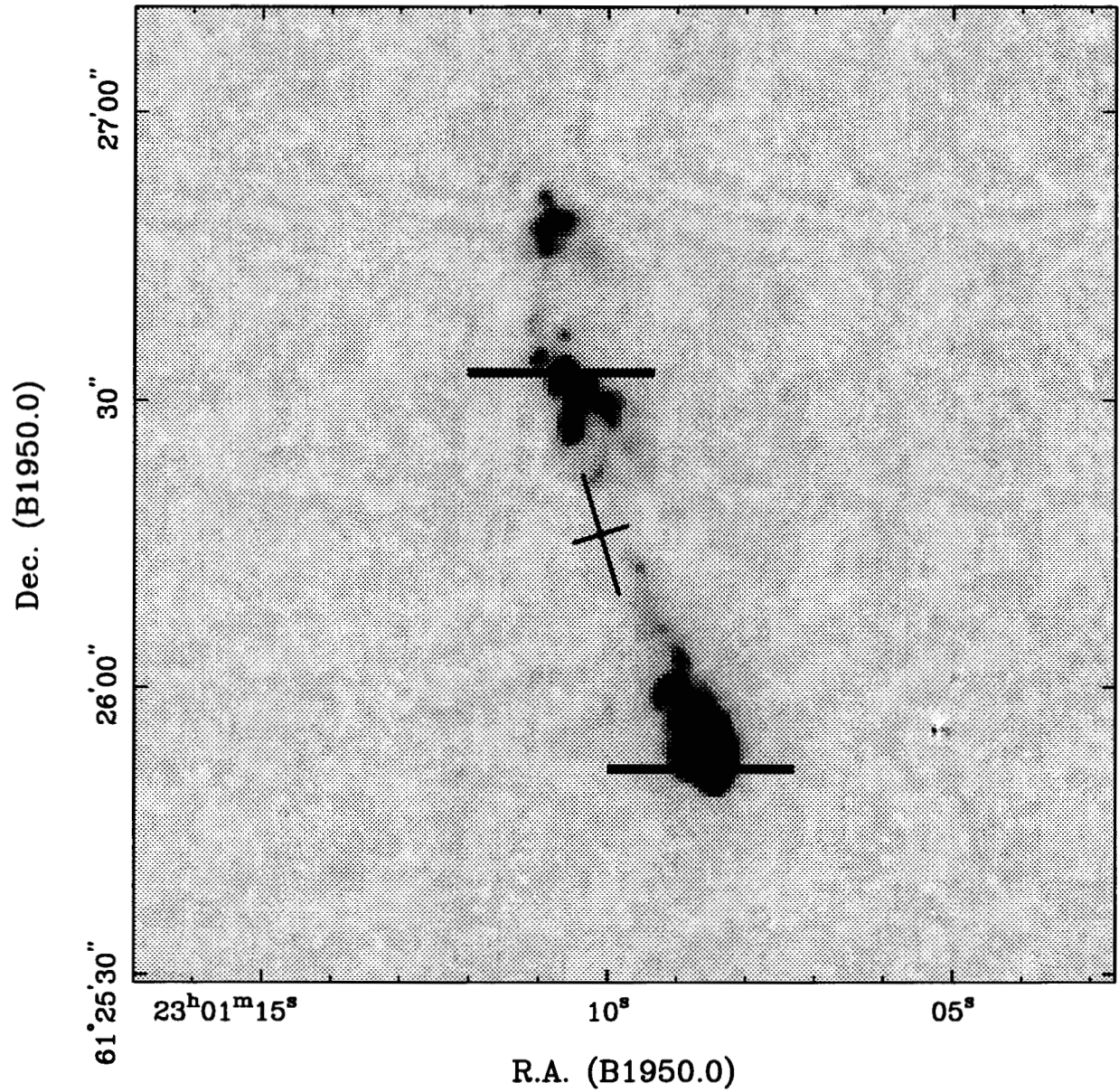


Fig. 1.— Grey-scale subsection of the H_2 at $2.12 \mu\text{m}$ continuum subtracted image around Cepheus E outflow region. The cross indicates the position of IRAS23011+6126 and it has a size comparable to that of IRAS uncertainty. The schematic slit positions for the infrared spectra discussed in the text are shown.

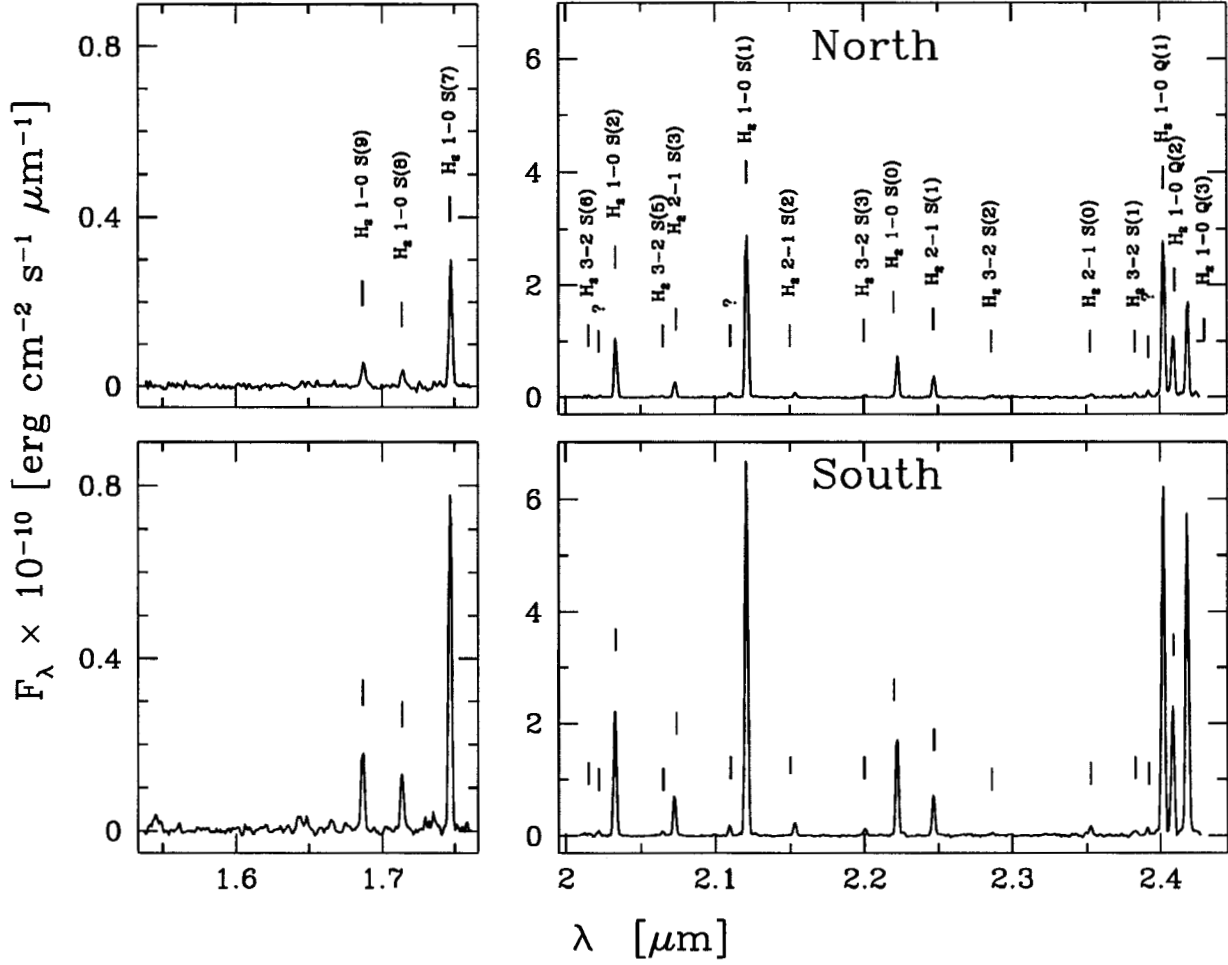


Fig. 2.— H and K band calibrated spectra of brightest knots of Cepheus E outflow. In (*top panel*) for northern lobe and (*bottom panel*) for the southern lobe. The wavelengths of the expected H₂ lines are marked. Note that Br γ line emission is not detected.

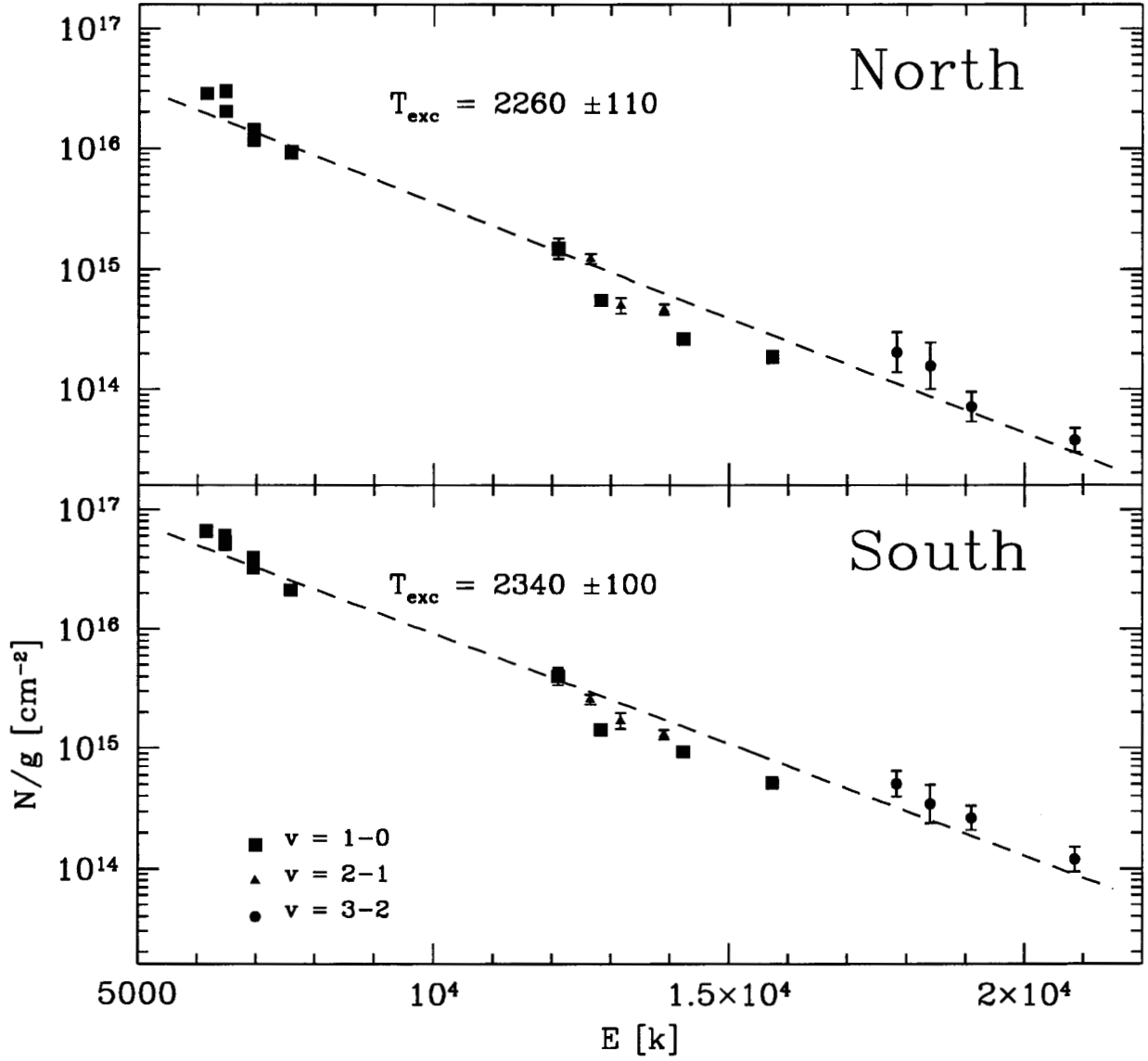


Fig. 3.— Excitation diagrams for the position on the brightest knots in Cepheus E lobes (shown in Figure 1). Different symbols have been employed for each vibrational level and are indicated in the bottom panel. The dashed lines are the least-square fit to all plotted transitions for the Northern lobe (*upper panel*) and the Southern lobe (*bottom panel*). The excitation temperature calculated for the fits is also indicated.

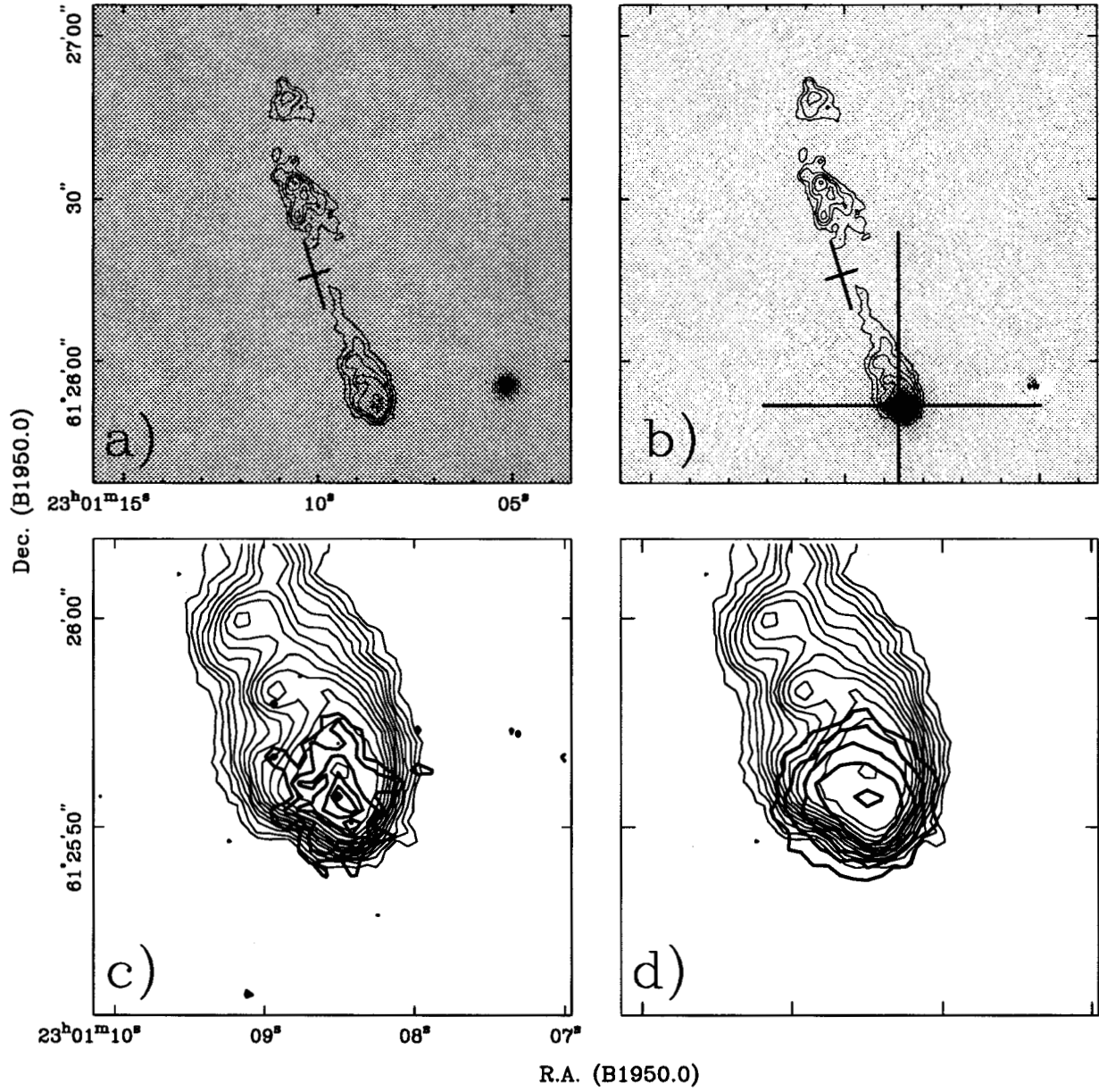


Fig. 4.— a) Contour map for the H $_2$ (1,0) S(1) continuum subtracted image (shown in Figure 1), overlaid on a grey-scale subsection of the H α continuum subtracted image of the region around Cepheus E. The contour interval is a logarithmic factor of 0.36. The cross indicates the IRAS23011+6126 position. b) The same H $_2$ (1,0) S(1) contour map (panel a) now overlaid on the grey-scale [S II] $\lambda\lambda 6717/31$ continuum subtracted image. This map shows the same image size than panel a). The right lines are the schematic slit positions for the optical spectra

discussed in this work. **c)** An overlay of the contour plots of the emission from a close-up of Cepheus E southern lobe showed in panel a (continuum subtracted). The dark contours represent the $H\alpha$ emission; the light contours represent the H_2 (1,0) S(1) emission. The contour interval increases linearly by a factor of the 1.1 for the $H\alpha$ map, and by a logarithmic factor of 0.13 for the infrared map. Note the spatial difference between the emission peak in $H\alpha$ and the corresponding peak in H_2 (1,0) S(1). **d)** An overlay of the contour plot of the images showed in panel b. The dark contours represent the $[S\ II]\ \lambda\lambda 6717/31$ emission; the light contours represent the H_2 (1,0) S(1) emission. In this case the contour interval for the $[S\ II]$ is a logarithmic factor of 0.17. This figure shows a clear offset between the $[S\ II]$ and the H_2 peak emissions.

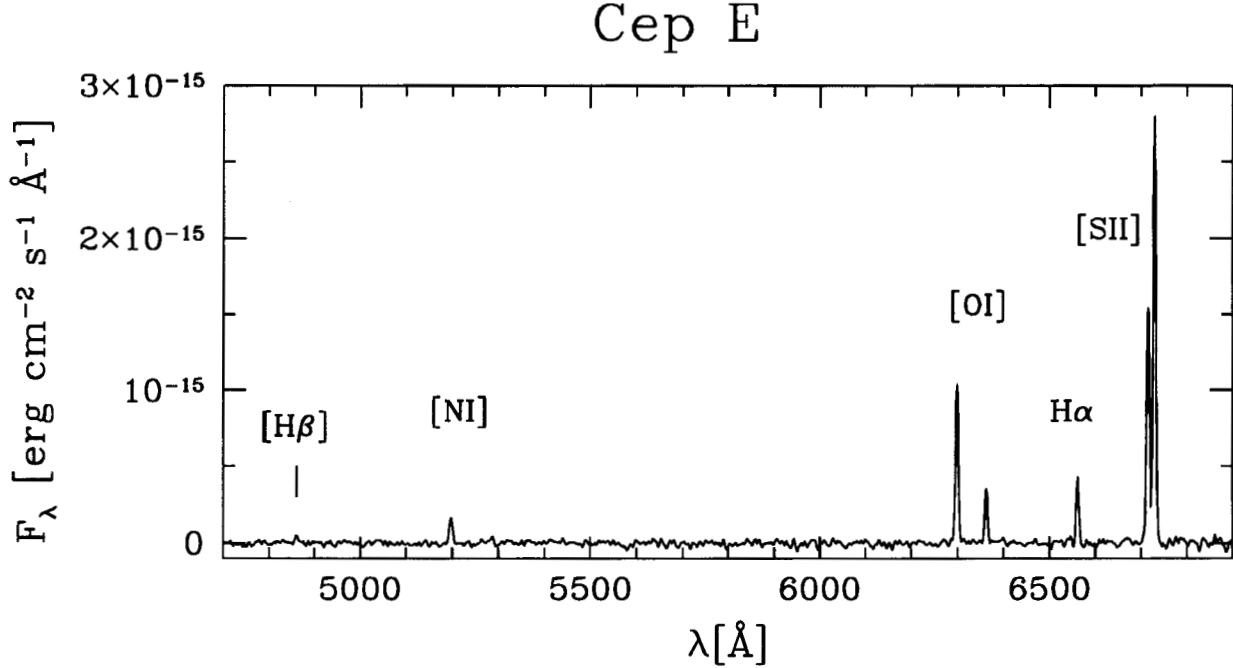


Fig. 5.— Low resolution spectrum of the Southern lobe in Cepheus E (named HH 377). The slit was E-W oriented as shown in Figure 4 (panel b). The measured fluxes are listed in column (2) on Table 4.

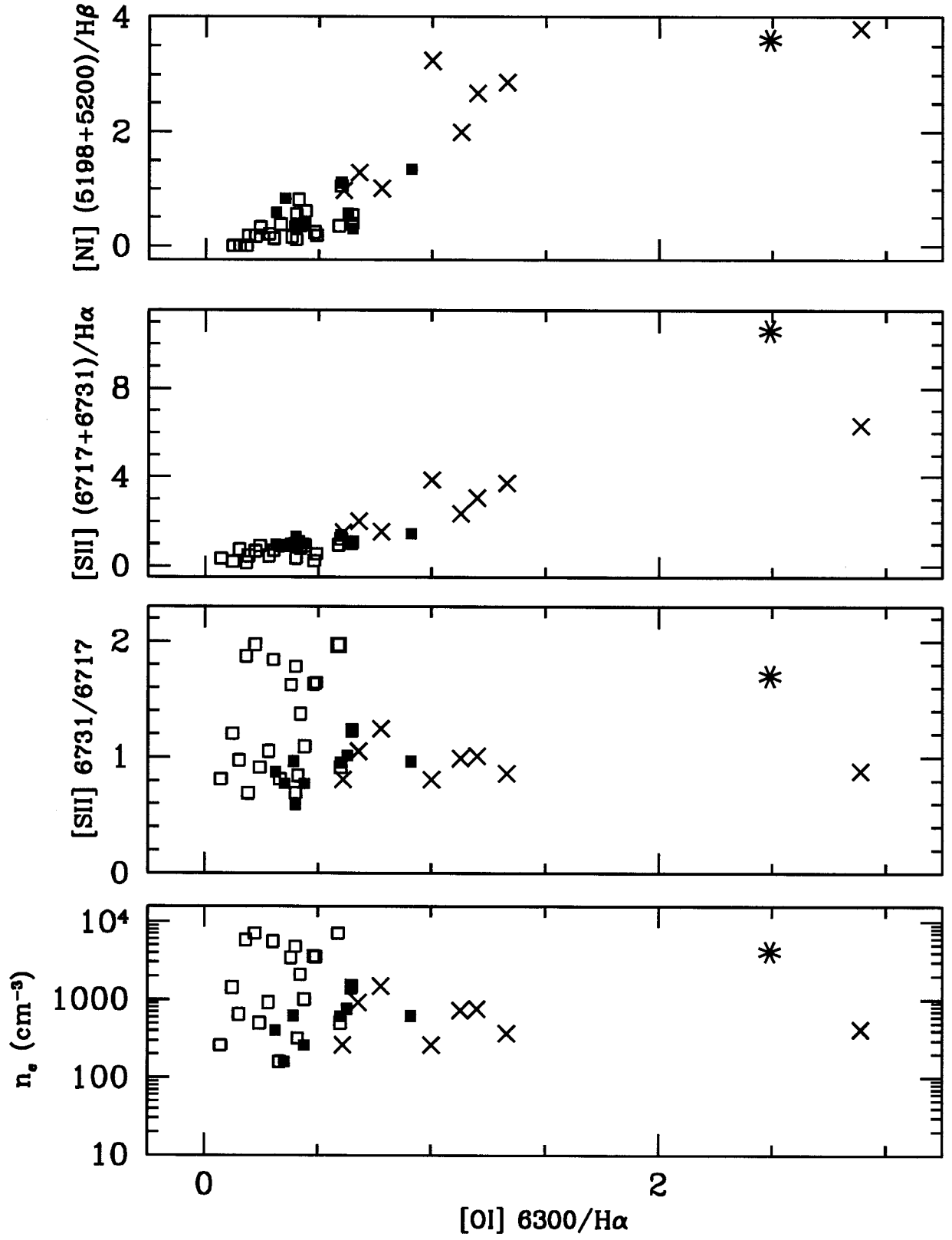


Fig. 6.— $[\text{NI}](5198+5200)/\text{H}\beta$, $[\text{SII}](6717+6731)/\text{H}\alpha$ and $[\text{SII}]6731/6717$ line ratios and electron density (n_e) as a function of $[\text{OI}]6300/\text{H}\alpha$ ratio. The objects with high excitation spectra are shown with open squares, the intermediate excitation spectra with solid squares, the low excitation objects with crosses, and Cepheus E with an asterisk.

TABLE 1

Imaging and spectroscopy observation log.

telescope ^a	date	filters/resolution	t_{exp} ^b
INFRARED			
Direct image			
APO 3.5m	18/07/96	2.12 μ m, 2.22 μ m	1800,190
OAN SPM 2.1m	08,09/01/97	cK, H ₂ 2.122 μ m, H ₂ 2.248 μ m, Br γ	540, 1080, 1080, 1260
Spectroscopy			
MMT	27/09/96	8 Å/pix	480
OPTICAL			
Direct image			
FLWO 1.2m	16/09/96	H α , [SII], [SII]Cont.	1800,1800,1800
Spectroscopy			
MMT	07/09/97	2 Å/pix	600
FLWO 1.5m	09/12/96	1.49 Å/pix	900
FLWO 1.5m	09/12/96	0.75 Å/pix	900

^aFLWO: Fred Lawrence Whipple Observatory, MMTO: Multiple Mirror Telescope, APO: Apache Point Observatory, OAN SPM: Observatorio Astronómico Nacional San Pedro Mártir

^bIntegration time in seconds

Table 1: Cepheus E H₂ line fluxes.

H ₂	λ	E(v', J')	$I_{v'J'}$	
transition	[μm]	[K]	$10^{-14} \text{ erg cm}^{-2} \text{ s}^{-1}$	
			North	South
(1)	(2)	(3)	(4) ^a	(5) ^a
(1,0) S(9)	1.6877	15735.1	1.90	5.22
(1,0) S(8)	1.7147	14232.7	1.13	3.95
(1,0) S(7)	1.7480	12827.9	8.01	20.64
(3,2) S(6)	2.0130	21911.0	0.52	0.64
(1,0) S(2)	2.0338	7590.8	24.27	56.14
(3,2) S(5)	2.0656	20856.0	0.54	1.74
(2,1) S(3)	2.0738	13902.0	6.03	17.61
(1,0) S(1)	2.1213	6957.2	72.50	166.30
(2,1) S(2)	2.1536	13161.4	1.80	5.90
(3,2) S(3)	2.2014	19102.0	0.90	3.32
(1,0) S(0)	2.2233	6476.8	17.18	43.84
(2,1) S(1)	2.2480	12650.7	8.51	17.65
(3,2) S(2)	2.2870	18401.4	0.52	1.14
(2,1) S(0)	2.3550	12105.1	1.74	4.66
(3,2) S(1)	2.3858	17833.2	1.37	3.40
(1,0) Q(1)	2.4066	6154.3	67.97	157.40
(1,0) Q(2)	2.4134	6471.2	27.96	56.85
(1,0) Q(3)	2.4237	6956.0	41.46	142.80
(1,0) Q(4)	2.4375	7590.8	2.39	...

^aFSPEC extraction region: $1'' \times 4''$. Measured uncertainties in the strong lines are typically $\pm 5\%$, and $\pm 20\%$ for the weak or poorly sky-subtracted lines.

Table 2: Derived Rotational Temperatures, Ortho/Para and (1,0)/(2,1) Ratios.

Vibrational Level	Transitions	T_{rot} [K]	Ortho/Para Ratio	(1,0)/(2,1) S(1)
(1)	(2)	(3)	(4)	(5)
Lobe North				
$v = 1 - 0$	S(1),S(2),S(3),S(7),S(8), S(9),Q(1),Q(2),Q(3)	1890 ± 90	2.99 ± 0.24	8.50 ± 1.10
$v = 2 - 1$	S(0),S(1),S(2),S(3)	1370 ± 320	4.73 ± 1.19	
$v = 3 - 2$	S(1),S(2),S(3),S(5)	1740 ± 250	2.66 ± 1.50	
Lobe South				
$v = 1 - 0$	S(1),S(2),S(3),S(7),S(8), S(9),Q(1),Q(2),Q(3)	1970 ± 80	2.96 ± 0.24	9.40 ± 1.30
$v = 2 - 1$	S(0),S(1),S(2),S(3)	1580 ± 190	2.99 ± 0.81	
$v = 3 - 2$	S(1),S(2),S(3),S(5)	2160 ± 110	2.98 ± 1.30	

Table 3: Observed(F)^a and Reddening-corrected^b (F_0) optical relative fluxes in Cepheus E.

Identification		F_λ					
		E-W ^c		N-S ^d		N-S ^e	
(1)		(2)		(3)		(4)	
		F	F_0	F	F_0	F	F_0
4861.3	H β	100	100
5199.3	[N I]	360	268
6300.2	[O I]	249	282	210	230	230	252
6363.9	[O I]	82	91	55	59	92	100
6562.8	H α	100	100	100	100	100	100
6716.4	[S II]	392	372	293	269	335	324
6730.8	[S II]	667	628	490	444	514	484
	$F(H\alpha)^f$	3.20	28.5	3.24	29.2	0.28	2.5
	$F(H\beta)^f$	0.42	10.1

^a[NI] line is normalized to $H\beta$ -flux equal 100, the other red lines are normalized to $H\alpha$ -flux equal 100.

^bCorrected using the reddening curve of Mathis (1990) and $E(B - V) = 0.88$, see text.

^cExtraction region $1.5'' \times 4''$. Measured uncertainties are less than 10%

^dExtraction region $1.5'' \times 6.8''$. Measured uncertainties are less than 15%

^eExtraction region $5'' \times 6.8''$. Measured uncertainties are less than 20%

^fin units of $10^{-15} \text{ erg cm}^{-2} \text{ s}^{-1}$

Table 4: Observed optical relative fluxes of HH377 and some shock models.

Object	$H\alpha/H\beta$	6717/6731	[NI]5200/ $H\beta$	[OI]6300/ $H\alpha$	[SII]/ $H\alpha$
(1)	(2)	(3)	(4)	(5)	(6)
Cep E	7.75	0.59	3.60	2.49	10.59
J4.20-30 ^a	5.3-8.4	0.7-1.4	2.0-90.	1.2-11.	2.9-58.
J4.30-40 ^a	4.0-6.1	0.5-1.2	0.2-5.6	0.5-2.0	0.5-5.0
J2.30-40 ^b	4.0-6.3	0.4-1.4	0.5-7.0	0.4-4.0	1.0-7.0

^aPlanar radiative shock models with v_s between 20-30 $km s^{-1}$ (J4.20-30) and 30-40 $km s^{-1}$ (J4.30-40). The $n_0 = 10^4 cm^{-3}$ and $B=30-300 \mu G$ (Hartigan et al., 1994)

^bPlanar radiative shock models with v_s between 30-40 $km s^{-1}$. The $n_0 = 10^2 cm^{-3}$ and $B=30-300 \mu G$ (Hartigan et al., 1994)